THE JOURNAL OF PHYSICAL CHEMISTRY C
A JOURNAL OF THE AMERICAN CHEMICAL SOCIETY

pubs.acs.org/JPCC

Article

Underlying Mechanisms of Hot Carrier-Driven Reactivity on Bimetallic Nanostructures

Zhandong Li, Joel Rigor, Nicolas Large, Patrick Z. El-Khoury, and Dmitry Kurouski*

Cite This: *J. Phys. Chem. C* 2021, 125, 2492–2501

Read Online

ACCESS | Metrics & More | Article Recommendations | Supporting Information

ABSTRACT: Bimetallic nanostructures exhibit unique catalytic activity and selectivity that are not evident for their monometallic analogues. Such nanostructures contain plasmonic metals, such as gold or silver, which afford highly efficient harvesting of electromagnetic radiation and its conversion into hot carriers. These highly energetic species are transferred to the catalytic metal subcomponent of the bimetallic nanostructure, where a large spectrum of chemical reactions may be catalyzed. The strength of the electric field and the interplay between catalytic and plasmonic metals at the nanoscale are thus critically important for the catalytic activity of bimetallic nanostructures. In this study, we investigate the relationship between the catalytic activity and local electric fields sustained on the surface of gold−palladium (Au@PdNPs) and gold−platinum (Au@PtNPs) nanoplates using tip-enhanced Raman spectroscopy. We image the spatially varying magnitudes of rectified (DC) local electric fields on the surface of these nanostructures and compare them to the fields sustained on the surface of monometallic nanoplates. We find substantially larger electric field magnitudes on Au@PdNPs and Au@PtNPs as compared to their monometallic analogues. These findings suggest that catalytic efficiency of bimetallic nanostructures may be mediated and potentially tuned through precise control of electric fields sustained on their surfaces.

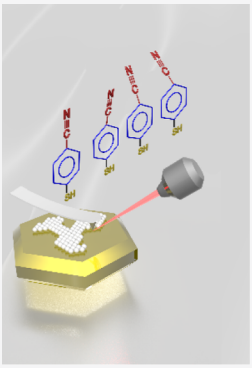

INTRODUCTION

Platinum (Pt) and palladium (Pd) metals are commonly used to catalyze various classes of chemical reactions.[1] The catalytic performance of these two metals can be significantly boosted by coupling them with plasmonic metals, such as gold (Au), silver (Ag), or aluminum (Al).[1−4] When catalytic and plasmonic metals are co-assembled or otherwise forged into a single nanostructure, their catalytic efficiency can be significantly enhanced.[5−7] Namely, the plasmonic metals in such nanostructures harvest electromagnetic radiation, converting it into localized surface plasmon resonances (LSPRs).[8−10] LSPRs decay through different mechanisms to form hot carriers.[11−14] These energetic species are then transferred to the catalytic metals, where they have been shown to accelerate the rates of several classes of chemical reactions.[15−19] Wang and co-workers reported direct harvesting of visible-to-near-infrared light for Suzuki coupling using plasmonic Au@Pd nanorods.[20] They found a two-fold enhancement in the reaction rate and product yield compared to the rate and yield reported for monometallic Pd nanostructures. The interplay between plasmonic and catalytic metals in such nanostructures is critically important. Lou and co-workers investigated the rates of hydrogen generation on three anisotropic Pt-covered, Pt-edged, and Pt-tipped Au triangular nanoprisms (TNPs).[21] They reported that Pt-edged TNPs exhibited nearly a three-fold and five-fold higher H_2 generation efficiency than the Pt-tipped and Pt-covered TNPs, respectively. The use of bimetallic nanostructures also enables green synthesis in organic chemistry, in part because such reactions are driven by electromagnetic radiation.

Plasmonic bimetallic nanostructures exhibit unique catalytic selectivity, which allows for the synthesis of desired products with optimal yields.[2,5,22] We previously showed that gold−platinum and gold−palladium nanoplates (Au@PtNPs and Au@PdNPs, respectively) not only enhanced reaction rates but also provided reaction selectivity that was not evident for the corresponding monometallic analogues.[23,24] Specifically, the Au@PtNPs enabled stepwise oxidation of 4-aminothiophenol (4-ATP) first to 4-nitrobenzenethiol (4-NBT) and then to *p,p′*-dimercaptoazobisbenzene (DMAB), whereas on their monometallic analogues, Au nanoplates (AuNPs), plasmon-driven oxidation of 4-ATP yielded only DMAB.[23] We also found that plasmon-driven reduction of 4-NBT on gold-platinum microplates yielded both DMAB and 4-ATP, whereas the monometallic microplates were able to produce only DMAB as a result of such photocatalytic reduction of 4-NBT.[24] We hypothesized that the observed reaction selectivity of both Au@PtNPs and Au@PdNPs is determined by the strength of the electric field and the interplay between catalytic

Received: January 7, 2021
Revised: January 12, 2021
Published: January 25, 2021

and plasmonic metals at the nanoscale. Based on this premise, one can expect that reaction selectivity on Au@PtNPs and Au@PdNPs may be controlled by external electric fields.

Here, we utilize tip-enhanced Raman spectroscopy (TERS) to visualize the magnitudes of local electric fields atop Au@PtNPs and Au@PdNPs. TERS is a near-field optical technique that has an angstrom-scale spatial resolution and single-molecule sensitivity under optimized conditions.[25−30] Over the last decade, TERS has been broadly used for elucidation of mechanisms of plasmon-driven and electrochemical reactions, as well as for structural characterization of biological and polymer specimens.[31−37] For instance, Weckhuysen and Deckert used TERS to monitor 4-NBT to DMAB conversion on the surface of AuNPs.[38] The Ren and Zenobi groups used TERS to probe the catalytic activity of Pd nanoislands on the surface of Au crystals.[39,40] They found that the edges of Pd islands exhibited higher reactivity relative to Pd atoms at the center of such islands.[40] Their recent findings showed that plasmon-driven reduction may take place not only on the catalytic metal islands, but also on the Au surface in the close proximity to the catalytic metal.[39] Our group previously showed that TERS could be used to reveal plasmon-driven reactivity on three different crystal facets of Au microplates.[41] We found that Au(111) crystal facets exhibited much higher catalytic reactivity when compared to Au(110) and Au(100). Schultz and co-workers proposed to use 4-mercaptobenzonitrile (4-MBN) as a molecular reporter that can gauge the absolute magnitudes of rectified local electric fields in SERS.[42,43] Namely, AC plasmons are rectified at plasmonic junctions,[44] and the local DC field magnitude can be gauged by monitoring vibrational Stark shifts in the C≡N resonance. In these measurements, Schultz and Marr observed both red-shifted and blue-shifted C≡N vibrational resonances in spectroscopic investigations of aromatic nitrile-functionalized SERS substrates and nanoparticles.[42] Using a similar approach, but now in the TERS geometry, El-Khoury and co-workers quantified the spatially varying magnitudes of rectified local optical fields. Upper limits for the magnitudes of rectified local optical fields in the TERS geometry were set for monometallic plasmonic nanoplates and nanoparticles, including Au nanoplates (42 MV·cm^{-1}),[45] spherical gold nanoparticles (38 MV·cm^{-1}),[46] gold nanocubes (32 MV·cm^{-1}),[47] and highly corrugated plasmonic nanotips (48 MV·cm^{-1}).[48] For a more detailed account of the aforementioned observables, the reader is referred to a recent perspective article by El-Khoury and Schultz.[49] With this information in hand, we herein use TERS to further understand the interplay between local optical fields and chemical reactivity in bimetallic gold nanoplates.

EXPERIMENTAL SECTION

Chemical Agents. Gold(III) chloride trihydrate ($HAuCl_4 \cdot 3H_2O$, 99.9%), palladium(II) chloride solution (H_2PdCl_4), chloroplatinic acid solution (H_2PtCl_6), hexadecyltrimethylammonium bromide (CTAB, 99%), mercaptobenzonitrile (4-MBN), sodium hydroxide (NaOH, 98%), potassium iodide (KI, 99%), L-ascorbic acid (AA, 99%), and sodium borohydride ($NaBH_4$, 99%) were purchased from Sigma-Aldrich (St. Louis, MO). Sodium citrate dihydrate (Na-Cit, 99%) was purchased from Fisher scientific (Waltham, MA). Ethanol was purchased from Decon Labs (King of Prussia, PA). All chemicals were used as received without purification.

Sample Preparation (AuNPs, Au@PdNPs, and Au@PtNPs). In our previous report, we have shown that TERS on AuNPs exhibit height dependence, whereas thicker nanoplates bring stronger enhancement because of the so-called gap-mode enhancement effect. Weak enhancement is expected if nanoplates thinner than 30 nm are used, let alone the observation of plasmonic catalyzation. Ideally, thicker nanoparticles should be prepared and used for TERS and further catalyzation. Other groups have shown the possibility of preparing both 70 nm thick AuNPs by isotropic growth and Au@PdNPs and Au@PtNPs *via* galvanic replacement. However, the preparation of bimetallic nanoparticles with height above 60 nm has never been achieved. For preparing all these nanoparticles, a three-step method was employed to get different products. AuNPs (15 nm thick) were prepared *via* seed-mediated growth and then used as the seed for preparing 70 nm AuNPs by isotropic growth. Then, the 70 nm AuNPs were exposed to Pt/Pd ions, allowing for the adlayer of Pt/Pt nanostructures on the surface of AuNPs. Considerable enhancement and distinguished catalytic capabilities have been shown on AuNPs, Au@PdNPs, and Au@PtNPs. First, Au seeds were synthesized by adding 0.01 M, 2 mL of $HAuCl_4$ and 0.01 M, 1 mL of Na−Cit solutions into 36 mL of water. Ice-cold 0.1 M, 1 mL $NaBH_4$ was prepared and added to the above solution under vigorous stirring for 2 min. The Au seed solution will be ready for use until the above mixture was kept at room temperature and aged for over 2 h. A solution of thin triangular or hexagonal AuNP seeds (∼15 nm thick) was then prepared by a three-step seed-mediated growth process from the Au seeds (after the seeds finished aging). Three growing solutions were prepared in three flasks labeled 1, 2, and 3. Growing solutions 1 and 2 were prepared following the same protocol: 0.05 M, 9 mL of CTAB solution was prepared in these two flasks and then 0.01 M, 0.25 mL of $HAuCl_4$, 0.1 M, 0.05 mL of NaOH, 0.01 M, 0.05 mL of KI, and 0.1 M, 0.05 mL of ascorbic acid (AA) were added in order. Then, the third growing solution was prepared in a larger quantity (10×) than solutions 1 and 2. Similarly, 0.01 M, 2.5 mL of $HAuCl_4$, 0.1 M, 0.5 mL of NaOH, 0.01 M, 0.5 mL of KI, and 0.1 M, 0.5 mL of AA were added into 0.05 M, 90 mL of CTAB solution. Then, 1 mL of the abovementioned Au seeds stocking solution was added into growing solution 1, followed by gently shaking for 5 s. Then, 1 mL of the mixture of Au seeds and growing solution 1 was added to growth solution 2, followed by gently shaking for another 5 s. Subsequently, all of the Au seeds and the mixture of growth solutions 1 and 2 in flask 2 were added to growing solution 3, followed by gently shaking for 5 s. The final solution was then kept undisturbed at room temperature for over 12 h. Then, after removal of the supernatant, ∼15 nm AuNPs seeds were redispersed and collected by precipitating at 5000 rpm for 2 min and dissolved in 5 mL of a 0.1 M CTAB solution to serve as seeds for the isotropic growth in the next step. The 70 nm AuNPs were then prepared by conducting isotropic growth with ∼15 nm AuNPs as seeds in a diluted 0.01 M CTAB solution. The growth solution was first prepared for isotropic growth. Briefly, 0.25 M, 1 mL of $HAuCl_4$, 0.1 M, 0.055 mL of AA, and water (8 mL) with 0.1 M, 1 mL of CTAB solution were mixed in order in the flask. Then, 0.25 mL of the 15 nm AuNPs seed solution was added to the abovementioned mixture in the flask to initialize the isotropic growth reaction. Subsequently, the expected thickness of AuNPs was at least 70 nm. For bimetallic nanoparticles, Au@PtNPs and Au@PdNPs were both synthesized by galvanic replacement following a similar protocol, and 60 μL of 20 mM AA was first added into 250 μL of the 70 nm AuNPs stock solution and mixed by

https://dx.doi.org/10.1021/acs.jpcc.1c00155
J. Phys. Chem. C 2021, 125, 2492−2501

vortexing for 10 s. Then, 15 μL, 10 mM of H_2PtCl_6 was introduced followed by vortexing for 10 s. The solution was kept at room temperature undisturbed for 1 h, allowing for the completion of bimetallic nanoplates' growth. The solution was centrifuged twice for 2 min at 8000 rpm for purification. Finally, after removal of the supernatant, the Au@PtNPs were dissolved in 1.0 mL of water and sonicated for 20 s. Similarly, 30 μL, 10 mM of H_2PdCl_4 was introduced to the mixture of 70 nm AuNP stock solution and 60 μL of 20 mM AA, following the same purification process and redispersed in 1.0 mL of water.

Modification of the 4-MBN on AuNPs/Au@PdNPs/Au@PtNPs. A fresh silicon wafer was cut into small squares of about 5 × 5 mm each. After sonicating in acetone and ethanol, all the small wafers were dried by nitrogen gas before use. The particles of the as-prepared AuNPs/Au@PdNPs/Au@PtNPs in stock solution were then dropped on the precleaned Si wafer and kept at room temperature for 30 min, allowing for the adsorption of nanoparticles on the surface. Then, the nanoplate-deposited Si wafer was immersed in a 2 mM ethanolic 4-MBN solution for 1 h to form a monolayer of 4-MBN on the surfaces of these nanoparticles *via* thiol-gold chemistry. The 4-MBN-modified sample was then sonicated in ethanol for 5 min to remove the uncoordinated 4-MBN molecules.

Metal deposition of Gold-Coated Tips. Silicon AFM probes with Al on reflex side, force constant 2.0 N/m, and resonance frequency 70 kHz were purchased from the NanoAndMore USA Corporation (Watsonville, CA). For gold coating, in brief, 10 sets of clamping devices were prepared for fixing the tips. Each device was then loaded with two tips and loaded into the thermal evaporator chamber (MBrown, Stratham, NH). Before the deposition starts, the chamber was allowed to evacuate to ~9×10^{-7} mbar. The inner pressure was kept at ~9×10^{-7} mbar or below during the deposition. Then, with increasing heat, gold pellets (Kurt J. Lesker, Efferson Hills, PA) thermally melted and evaporated at a constant 0.1−0.2 Å·s^{-1} rate. After 70 nm of Au was deposited on the AFM tips, the evaporation was stopped and kept cooling down to room temperature. The temperature at the tip surface and deposition chamber was ~50 °C.

TERS Instrument Setup. The AIST-NT-HORIBA system equipped with a 632.8 nm continuous wavelength (CW) laser was used for atomic force microscopy (AFM) scanning experiments, AFM-TERS, and spectrum collections. A laser light was brought to the sample surface in a side-illumination configuration with a 100× Mitutoyo microscope objective. The scattered electromagnetic radiation was also collected with the same objective and directed into a fiber-coupled Horiba iHR550 spectrograph that is equipped with a Synapse EM-CCD camera (Horiba, Edison, NJ). According to our estimate, the laser spot in our TERS system is around 0.3 mm in diameter, which provides the following power densities: 0.04 W/cm^2 at 30 μW, 0.13 W/cm^2 at 90 μW, and 0.21 W/cm^2 at 150 μW.

Scanning Electron Microscopy Characterization. Scanning electron microscopy (SEM) characterization of AuNPs/Au@PdNPs/Au@PtNPs was conducted using a JEOL scanning electron microscope (JSM-7500F).

RESULTS AND DISCUSSION

Vibrational Stark Nanoscopy on Au@PdNPs. We coated Au@PtNPs and Au@PdNPs with a monolayer of 4-MBN to probe the spatial distribution of rectified electric fields on the surface of these bimetallic nanostructures. Au@PtNPs and Au@PdNPs were prepared in three steps as illustrated in Figure 1A (see details in Supporting Information). Briefly, 15

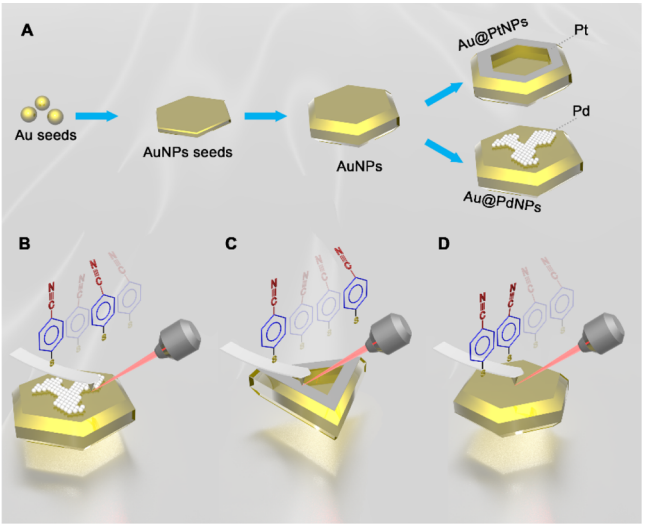

Figure 1. Nanoscale catalytic properties of mono- and bimetallic nanostructures revealed by TERS. (A) Synthetic approach for preparation of AuNPs, Au@PtNPs, and Au@PdNPs. Nanoscale TERS imaging of the rectified DC field of 4-MBN on (B) Au@PdNPs and (C) Au@PtNPs, compared to the increase in electric field strength on (D) AuNPs.

nm thick AuNPs are prepared via seed-mediated growth and then isotropic growth from 15 nm (Figure S1) AuNPs to 70 nm (Figure S2). Finally, 70 nm AuNPs are exposed to the Pt and Pd ions to allow for the formation of random islands of Pd (~1 nm in height, see Figure S3) on Au@PdNPs and Pt around the perimeter of Au@PtNPs (see Figure S4). The lateral dimensions of AuNPs, Au@PtNPs, and Au@PdNPs are all in the 200−300 nm range (Figure S5), which make them ideal for the elucidation of spatially varying local electric fields as gauged through the vibrational Stark effect. The TERS spectra of 4-MBN on Au@PdNPs (Figure 2A) exhibit four distinct vibrational bands at 1076, 1183, 1585, and 2225 cm^{-1}. The first three bands correspond to the vibration modes of the benzene rings, whereas the bands at around 2225 cm^{-1} correspond to the vibration of C≡N.

We found that in some of the collected TERS spectra from the surface of Au@PdNPs, only the band at 2225 cm^{-1} was shifted to 2208−2210 cm^{-1} (Figures 2A and S6), which is consistent with prior SERS and TERS works that utilized the C≡N moiety of 4-MBN as a probe of local DC fields. These blue shifts indicate site-specific increases in the magnitudes of rectified local electric fields on the surface of Au@PdNPs. Our experimental results show that an increase in the laser intensity further increases the magnitude of the Stark shift, shifting the C≡N resonance to 2195 and 2179 cm^{-1} at 90 and 150 μW, respectively. To first order, the change in vibrational frequency (Stark shift) induced by an electric field may expressed as

$$\Delta\nu = -\Delta\mu_{C\equiv N}\cdot\Delta E \quad (1)$$

where $\Delta\nu$ is the Stark shift, $\Delta\mu_{C\equiv N}$ = 0.6 cm^{-1}/(MV/cm) is the Stark tuning rate for 4-MBN,[48] and ΔE is the change in the strength of the rectified local optical field in the TERS geometry.[50] This allows us to directly infer the magnitudes of

https://dx.doi.org/10.1021/acs.jpcc.1c00155
J. Phys. Chem. C 2021, 125, 2492−2501

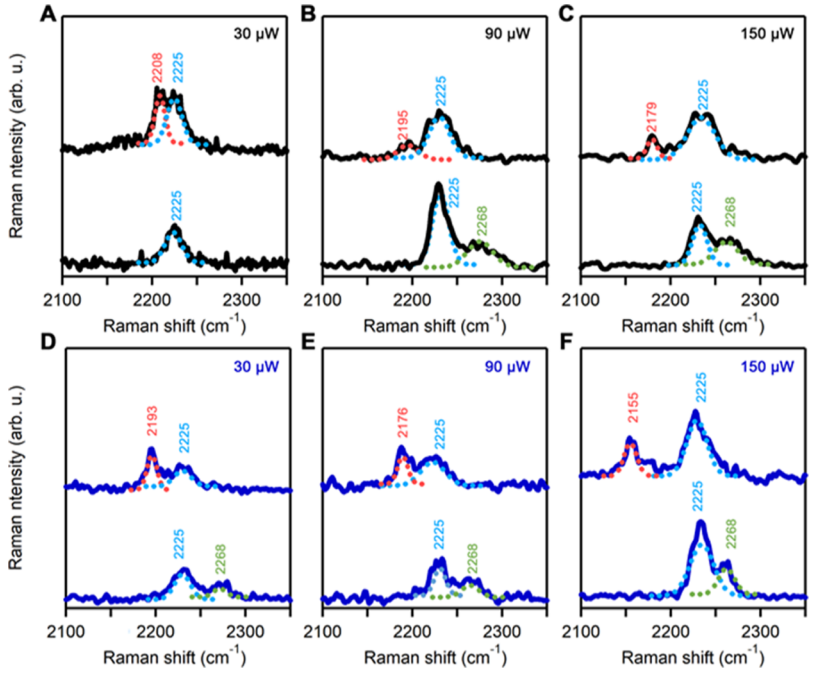

Figure 2. Representative Stark-shifted TERS spectra of 4-MBN on Au@PdNPs and Au@PtNPs. TERS spectra collected from Au@PdNPs exhibit a blue Stark shift of the vibration band at 2225 cm^{-1} (blue dashed line). The Stark-shifted band (red dashed line) appears at (A) 2208 cm^{-1} at 30 μW, (B) 2195 cm^{-1} at 90 μW, and (C) 2179 cm^{-1} at 150 μW. At 90 μW (B) and 150 μW (C), we also observed the formation of a vibrational band at 2268 cm^{-1} (green dashed line), which originates from the red Stark shift of 4-MBN. TERS spectra (A−C) are randomly picked from TERS images of Au@PdNPs shown in Figure 3. TERS spectra collected from Au@PtNPs exhibit a blue Stark shift of the vibration band at 2225 cm^{-1} (blue dashed line). The Stark-shifted band (red dashed line) appears at (D) 2193 cm^{-1} at 30 μW, (E) 2176 cm^{-1} at 90 μW, and (F) 2155 cm^{-1} at 150 μW. At 30 μW (D), 90 μW (E), and 150 μW (F), we observed the formation of a vibrational band at 2268 cm^{-1} (green dashed line), which originates from red Stark shift of 4-MBN. TERS spectra (D−F) are randomly picked from TERS images of Au@PtNPs shown in Figure 3.

the rectified electric fields at the surface from the spectral shifts. From the Stark shifts reported above, we obtained electric field changes of −50 and −76.6 MV·cm^{-1}, respectively. TERS imaging of the Au@PdNPs with optical powers of 30−90 μW revealed that blue shifts occurred primarily at the edges of the Pd nanoislands (Figure 3C−E, red spots). At higher optical powers (90−150 μW), we observed the blue shifts on both edges and top surfaces of the Pd nanoislands. We also found that the surface area of the corresponding enhanced electric field locations on the surface of Au@PdNPs increases with increasing laser powers. At low laser powers, only a small number of locations that exhibit enhanced electric field are observed. With an increase in the energy of the incident laser, the number of sites at which the field is rectified is drastically increased.

Our experimental results show that TERS spectra collected from Au@PdNPs at 90 and 150 μW also exhibited a vibrational band centered around 2268 cm^{-1} (Figure 2B,C), whereas this band was not observed in any spectra collected at 30 μW (Figure 2A). The Ren group previously reported that the appearance of such a band corresponds to the formation of nitric oxide (N═C═O).[40] Nonetheless, the catalytic conversion of 4-MBN to 4-mercaptobenzonitric oxide (4-MBNO) is precluded on the basis of density functional theory calculations of 4-MBNO (Figure S7). Interestingly, we find that the vast majority of the acquired TERS spectra exhibit either blue-shifted or red-shifted nitrile resonances, but not both simultaneously. This observation was rationalized in a prior work, whereby both higher-frequency and lower-frequency vibrational resonances on locally corrugated plasmonic nanostructures were contracted with strictly unidirectional Stark shifts on nanometrically smooth plasmonic nanoparticles.[48] By recognizing that the Stark tuning rates and local fields are signed quantities, both red- and blue-shifted Stark-tuned resonances require a change in local field polarity, which is likely driven by contact potential variations within the tip and bimetallic nanoplate nanocorrugations. Recognizing that the tuning rate is positive when the field is pointing from the tip to monometallic nanoplates,[45,48] we can associate the observation of red-shifted resonances on the bimetallic plates with a switch in the direction of the rectified local field. Specifically, the field now points from the nanoplate to the tip in the latter scenario.

Vibrational Stark Nanoscopy on Au@PtNPs and AuNPs. Similar behavior of the nitrile vibration has been observed on Au@PtNPs. However, we observed a larger rectified electric field on their surface at these laser powers. For instance, at 30 μW, we found that the 2225 cm^{-1} band appeared to be shifted to 2193 cm^{-1} on Au@PtNPs, which corresponds to a field magnitude of −53.3 MV·cm^{-1}. Au@PdNPs supported fields on the order of −28.3 MV·cm^{-1} ($\Delta\nu$ = 17 cm^{-1}) under the same experimental conditions. At an optical power of 30 μW, we also observed the red-shifted nitrile resonances on Au@PtNPs, which were not evident for Au@PdNPs. It should be noted that for Au@PtNPs, the red-shifted nitrile resonance was observed around the perimeter of the Pt rim on the bimetallic nanostructures. Similar areas that exhibit negative Stark shifts on Au@PtNPs remain nearly the same at 30, 90, and 150 μW. However, the magnitudes of the shifts increase with the laser power. Specifically, the −32 cm^{-1} shift (−53.3 MV·cm^{-1}), which was observed at 30 μW, increased to 49 cm^{-1} at 90 μW and to 70 cm^{-1} at 150 μW

https://dx.doi.org/10.1021/acs.jpcc.1c00155
J. Phys. Chem. C 2021, 125, 2492−2501

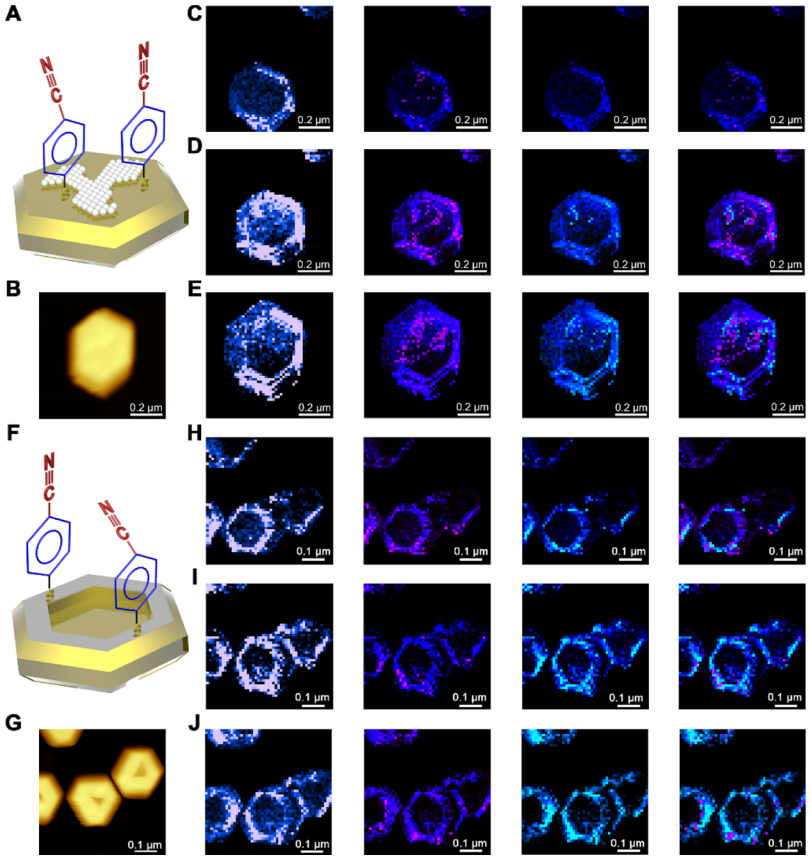

Figure 3. TERS mapping of 4-MBN on Au@PdNPs and Au@PtNPs. (A) Schematic illustration of 4-MBN on Au@PdNPs. (B) AFM image of Au@PdNP with 4-MBN on the surface that corresponds to TERS images of 4-MBN at (C) 30 μW, (D) 90 μW, and (E) 150 μW. Intensity of the vibration at 2225 cm^{-1} (C≡N stretching) is shown in blue, the Stark shift (2208−2179 cm^{-1}) is shown in red, and the 2268 cm^{-1} vibration that corresponds to red Stark shift of 4-MBN is in green. (F) Schematic illustration of 4-MBN on Au@PtNPs. (G) AFM image of Au@PtNP with 4-MBN on the surface that corresponds to TERS images of 4-MBN at (H) 30, (I) 90, and (J) 150 μW. Intensity of vibration at 2225 cm^{-1} (C≡N stretching) is shown in blue, the Stark shift (2193−2155 cm^{-1}) is shown in red, and the 2268 cm^{-1} vibration that corresponds to red Stark shift of 4-MBN is in green. The spatial imaging resolution is 10 nm in all maps.

(−81.7 and −116.7 MV·cm^{-1}, respectively). It is important to stress at this point that it is not clear to what extent the higher field values we derive (>50 MV·cm^{-1}) are "contaminated" by the formation of the anionic form of 4-MBN.[48] This will be the subject of follow-on reports from our group. Overall, similar to Au@PdNPs, we found very little, if any, overlap between sites that exhibited blue- and red-shifted nitrile resonances (3/3321 for Au@PtNPs and 2/1854 for Au@PdNPs at only 150 μW), which reinforces the previously painted picture of site-specific local field polarity switching.[48]

It should be noted that AuNPs exhibit drastically different behavior than both Au@PdNPs and Au@PtNPs. For instance, these nanostructures exhibited strictly unidirectional Stark shifts. Specifically, the nitrile vibration band has been found to red-shift from 2225 to 2231 cm^{-1} at 30 μW, to 2236 cm^{-1} at 90 μW, and to 2241 cm^{-1} at 150 μW (see Figure S8), which is in excellent agreement with previous works from Schultz and El-Khoury.[42,43,51] We also plotted the intensity of the C≡N vibration band as a function of the calculated electric field value for the three different laser powers (Figure 4). This figure allows for evaluating the uncertainty in the electric field that is inhomogeneously distributed on the surface of both mono- and bimetallic nanostructures.[42] The region between the two gray solid lines depicts the full range of electric field distributions (Figure 4). We found that the electric field distribution becomes narrower and more uniform with the laser power increasing from 30 to 150 μW (Figure 4A−C for Au@PdNPs, Figure 4D−F for Au@PtNPs, and Figures S9, S10 for AuNPs). This suggests that the increase in laser power results in lower heterogeneity of the electric field distribution on the surface of Au@PdNPs, Au@PtNPs, and AuNPs. We have also observed a logarithmic relationship between the laser power and the electric field on the surface of Au@PtNPs and Au@PdNPs, while it appeared hyperbolic in the case of AuNPs. Specifically, we observed a nearly two-fold increase in the electric field strength with an increase in the laser power from 30 to 90 μW for AuNPs, whereas subsequent increase in the laser power (from 90 to 150 μW) resulted in a statistically negligible increase of the electric field (Figure 4L). Interestingly, Au@PdNPs and Au@PtNPs exhibited the opposite behavior, where an increase in the electric field from 30 to 90 μW did not result in any significant change in the electric field on any of these bimetallic nanostructures. However, an increase from 90 to 150 μW induced a significant decrease in the electric field on Au@PdNPs and Au@PtNPs (Figure 4J,K).

We have calculated the probability of observing Stark-shifted resonances on Au@PtNPs and Au@PdNPs at three different laser powers (30, 90, and 150 μW) (Figure S11 and Table 1). On Au@PdNPs, the Stark shift events increased from 22.7 to 41.6% as the laser power changed from 30 to 150 μW. In comparison, the Stark shift events decreased from 16.5 to 9.5%

https://dx.doi.org/10.1021/acs.jpcc.1c00155
J. Phys. Chem. C 2021, 125, 2492−2501

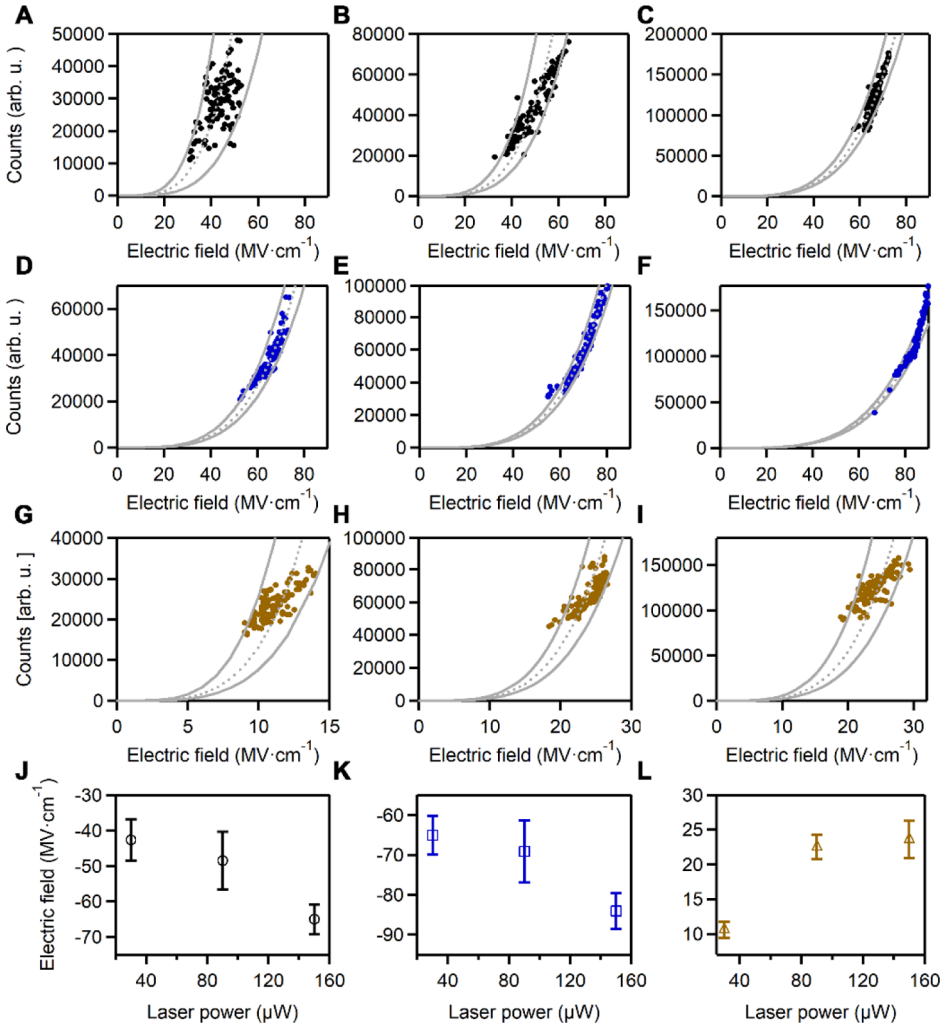

Figure 4. Electric field distribution on Au@PdNPs, Au@PtNPs, and AuNPs. Intensities of C≡N vibration plotted against the determined electric fields on Au@PdNPs at a laser power of (A) 30, (B) 90, and (C) 150 μW. Because the electric fields are calculated to have negative values for Au@PdNPs and Au@PtNPs, absolute values of the field change $|\Delta E|$ are used for the plotting; same for (D–F). Intensities of C≡N vibration plotted against the determined electric fields on Au@PtNPs at laser powers of (D) 30, (E) 90, and (F) 150 μW. Intensities of C≡N vibration plotted against the determined electric fields on AuNPs at laser powers of (G) 30, (H) 90, and (I) 150 μW. The gray lines are the AE^4 model fitted onto the data. The width between the fitting lines at two ends corresponding to the full width at half maximum of the C≡N stretch and the uncertainty in the electric field. In each plot from (A–I), A = 0.012, 0.011, 0.0095, 0.0086, 0.0081, 0.0074, 0.76, 0.13, and 0.20, respectively. Statistical analysis on the electric field distribution on (J) Au@PdNPs, (K) Au@PtNPs, and (L) AuNPs at different laser powers.

as the laser power changed from 30 to 150 μW on Au@PtNPs. Our results also show that an increase in laser power results in a decrease of the surface area that exhibits a Stark shift on Au@PtNPs. Surprisingly, the opposite trend has been observed on Au@PdNPs. However, this can be explained by the substantial difference in the magnitude of the electric field on the surface of Au@PtNPs and Au@PdNPs. Specifically, mean values of the electric field on Au@PtNPs vary from −65 MV·cm^{-1} at 30 μW to −69 MV·cm^{-1} and −84 MV·cm^{-1} at 90 and 150 μW, respectively. On the other hand, on Au@PdNPs, the field changes from −42 MV·cm^{-1} at 30 μW to −47 MV·cm^{-1} and −66 MV·cm^{-1} at 90 and 150 μW, respectively. Therefore, Au@PtNPs exhibit a stronger electric field at any given laser power compared to Au@PdNPs.

The observed relationship between the laser power and the area of surface sites that exhibit a Stark shift on Au@PtNPs and Au@PdNPs may suggest that the number of surface sites that exhibit a Stark shift could increase from 0 to 30 μW on Au@PtNPs and decrease at laser powers above 150 μW on Au@PdNPs. This hypothesis cannot be verified experimentally because (i) no TERS can be observed with optical powers lower than 30 μW and (ii) degradation of the apex nanostructure at the scanning probe is unavoidable for powers above 150 μW (with a 633 nm laser). Alternatively, one can expect that with an increase in the external electric field, the number of surface sites that exhibit a Stark shift on Au@PtNPs will change exponentially. In this case, an increase in the laser power will result in a continuous exponential decrease in the number of surface sites on Au@PtNPs. However, on Au@PdNPs, the number of such sites will continue increasing exponentially with the increase in the laser power. Quantum chemical calculations would be required to fully explain the observed difference between the Stark shift dependence on Au@PtNPs and Au@PdNPs.

We also performed electrodynamic simulations using the finite-difference time-domain method (FDTD, Lumerical DEVICE Suite) to investigate the LSPR properties of these mono- and bimetallic nanostructures (detailed in Supporting

https://dx.doi.org/10.1021/acs.jpcc.1c00155
J. Phys. Chem. C 2021, 125, 2492−2501

Table 1. Probability of Blue Stark Effect and Red Stark Effect of 4-MBN on Au@PdNPs, Au@PtNPs, and AuNPs

Nanostructures	Laser power	Blue Stark shift	Red Stark shift
 Au@PdNPs	30 μW	22.7%(349/1536)	–
	90 μW	34.1%(561/1647)	2.1%(35/1647)
	150 μW	41.6%(772/1854)	9.1%(168/1854)
 Au@PtNPs	30 μW	16.5%(537/3255)	28.4%(924/325)
	90 μW	12.1%(411/3386)	39.0%(1322/3386)
	150 μW	9.5%(316/3321)	49.5%(1644/3321)
 AuNPs	30 μW	8.6%(249/2894)	–
	90 μW	14.3%(395/2762)	–
	150 μW	30.9%(963/3115)	–

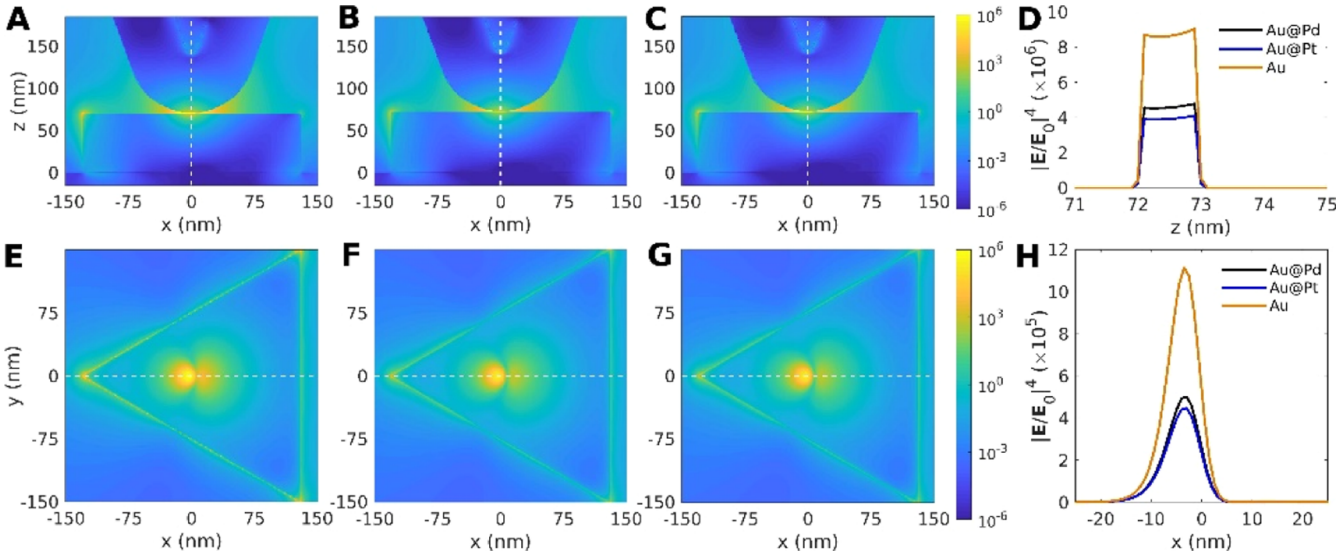

Figure 5. $|E/E_0|^4$ spatial distributions for AuNP, Au@PdNP, and Au@PtNP. (A–C) Cross-sectional (x,z) maps in the tip–substrate region of AuNP, Au@PdNP, and Au@PtNP, respectively. (D) Field profiles for the gap region, calculated along the z-axis (white dashed lines in panels A–C). (E–G) Cross-sectional (x,y) maps on the top surface of AuNP, Au@PdNP, and Au@PtNP, respectively. Each mapping is calculated at a single excitation wavelength of 633 nm. (H) Field profiles on the NP surface, calculated along the x-axis (white dashed lines in panels E–G).

Information). We modeled our three systems (AuNP, Au@PdNP, and Au@PtNP) as nanotriangles with lateral dimensions of 300 nm and a height of 70 nm. The experimental conditions have been taken into account in the simulations: an incident plane wave with a wavelength of 633 nm and an incidence of 45° from the z-axis (see Figure S12). Figure 5 shows the spatial distributions of the fourth power of the local electric field enhancement $|E/E_0|^4$. As it can be seen in Figure 5A–C, the strongest local electric field enhancement comes from within the gap region itself because of the strongly confined electromagnetic fields found between the tip apex and the surface of the substrate. This is attributed to the strong dipole–dipole interactions found between the LSPRs of the tip and of the NP. In comparison, we found that the AuNP has the strongest enhancement within the gap region as compared to the Au@PdNP and Au@PtNP cases. It is worth mentioning that this result is expected because of the damped plasmonic response from Pd and Pt.[52] In terms of catalysis, this shows that the AuNP would provide the best means of catalytic activity because of the diminished electric field produced by both the Au@PdNPs and Au@PtNPs. We also observe some strong local electric field near the edges of the NPs showing strong areas for catalytic activity. Figure 5E–G shows the top surface of the different NPs. We observe that the strongest local electric field comes from the area directly below the tip. Again, AuNPs have the strongest enhancement among the three systems and have a larger area where this enhancement occurs compared to Au@PtNPs and Au@PtNPs. Figure 5H shows the field profile across the tip–substrate region, as well as across the top surface of the NP. We observe the largest electric field strength produced within the gap region itself. We can also see the clear depression of the electric field due the addition of either Pd or Pt. While the electric field in the gap decreases by 47 and 54% (Figure 5D) for Au@PdNP and Au@PtNP, respectively, it actually experiences a stronger decrease at the surface (Figure 5H), which is of the order of 55 and 60%

https://dx.doi.org/10.1021/acs.jpcc.1c00155
J. Phys. Chem. C 2021, 125, 2492–2501

for Au@PdNP and Au@PtNP, respectively. These results point out the distinct behaviors of AC plasmons and rectified local DC fields on the surface of Au@PdNP, Au@PtNP, and AuNPs. The distinction is important in the quest to advance novel catalysts that take full advantage of the plasmonic enhancement.

CONCLUSIONS

Our results suggest that bimetallic plasmonic nanoplates have distinct properties compared to their monometallic analogues. In the context of using TERS to monitor chemical transformations at the surface of bimetallic catalysts, we uncover large rectified local electric fields that are operative and that may hold the key to rationalizing the high efficiency and unique selectivity of these constructs. It is important to distinguish between AC plasmons and rectified DC fields in this context. The former is well known, and these local optical fields are largely concentrated at the edges of plasmonic nanoplates. The rectified fields we observe, albeit potentially a consequence of our probing method of choice, strongly suggest that external electric fields can be used to tune the catalytic performance of bimetallic catalysts. On a final note, the use of power (of the incident laser) as a knob to control the number of sites that sustain large local electric fields is useful in the quest to drive and control nanochemistry, as probed through TERS.

ASSOCIATED CONTENT

Supporting Information

The Supporting Information is available free of charge at https://pubs.acs.org/doi/10.1021/acs.jpcc.1c00155.

Calculation details, electrodynamic simulations, AFM images and height profiles of different nanoplates, SEM images, representative TERS spectra, density functional theory calculations, histogram of the electric field distribution, mapping C≡N Stark shift on Au nanoplates, probability of blue/red Stark shift of 4-MBN on Au@PtNPs and Au@PdNPs at different laser powers, and the computational TERS model (PDF)

AUTHOR INFORMATION

Corresponding Author

Dmitry Kurouski − *Department of Biochemistry and Biophysics, Texas A&M University, College Station, Texas 77843, United States; The Institute for Quantum Science and Engineering, Texas A&M University, College Station, Texas 77843, United States;* orcid.org/0000-0002-6040-4213; Phone: 979-458-3778; Email: dkurouski@tamu.edu

Authors

Zhandong Li − *Department of Biochemistry and Biophysics, Texas A&M University, College Station, Texas 77843, United States*

Joel Rigor − *Department of Physics and Astronomy, The University of Texas at San Antonio, San Antonio, Texas 78249, United States*

Nicolas Large − *Department of Physics and Astronomy, The University of Texas at San Antonio, San Antonio, Texas 78249, United States;* orcid.org/0000-0002-2699-5718

Patrick Z. El-Khoury − *Physical Sciences Division, Pacific Northwest National Laboratory, Richland, Washington 99352, United States;* orcid.org/0000-0002-6032-9006

Complete contact information is available at: https://pubs.acs.org/10.1021/acs.jpcc.1c00155

Author Contributions

D.K. and Z.L. conceived the idea and designed the experiments; Z.L. synthesized and characterized nanoparticles; Z.L. performed all experimental measurements and analyzed the data; J.R. and N.L. developed the theoretical models and performed the FDTD simulations; P.E. performed DFT calculations; Z.L., J.R., N.L., P.E. and D.K. wrote the manuscript. All authors discussed the results and contributed to the final manuscript.

Notes

The authors declare no competing financial interest.

ACKNOWLEDGMENTS

D.K. is supported by AgriLife Research of Texas A&M and Governor's University Research Initiative (GURI) grant program of Texas A&M University (grant no. 12-2016, M1700437). This work received computational support from UTSA's HPC cluster SHAMU, operated by the Office of Information Technology. P.Z.E. acknowledges support from the US Department of Energy, Office of Science, Office of Basic Energy Sciences, Division of Chemical Sciences, Geosciences & Biosciences.

REFERENCES

(1) Sytwu, K.; Vadai, M.; Dionne, J. A. Bimetallic nanostructures: combining plasmonic and catalytic metals for photocatalysis. *Adv. Phys.* **2019**, *4*, 1619480.

(2) Zhou, L.; Martirez, J. M. P.; Finzel, J.; Zhang, C.; Swearer, D. F.; Tian, S.; Robatjazi, H.; Lou, M.; Dong, L.; Henderson, L.; et al. Light-driven methane dry reforming with single atomic site antenna-reactor plasmonic photocatalysts. *Nat. Energy* **2020**, *5*, 61−70.

(3) Brongersma, M. L.; Halas, N. J.; Nordlander, P. Plasmon-induced hot carrier science and technology. *Nat. Nanotechnol.* **2015**, *10*, 25−34.

(4) Zhang, C.; Zhao, H.; Zhou, L.; Schlather, A. E.; Dong, L.; McClain, M. J.; Swearer, D. F.; Nordlander, P.; Halas, N. J. Al−Pd nanodisk heterodimers as antenna−reactor photocatalysts. *Nano Lett.* **2016**, *16*, 6677−6682.

(5) Mukherjee, S.; Zhou, L.; Goodman, A. M.; Large, N.; Ayala-Orozco, C.; Zhang, Y.; Nordlander, P.; Halas, N. J. Hot-electron-induced dissociation of H2 on gold nanoparticles supported on SiO2. *J. Am. Chem. Soc.* **2013**, *136*, 64−67.

(6) Zhou, L.; Zhang, C.; McClain, M. J.; Manjavacas, A.; Krauter, C. M.; Tian, S.; Berg, F.; Everitt, H. O.; Carter, E. A.; Nordlander, P.; Halas, N. J. Aluminum nanocrystals as a plasmonic photocatalyst for hydrogen dissociation. *Nano Lett.* **2016**, *16*, 1478−1484.

(7) Ksar, F.; Ramos, L.; Keita, B.; Nadjo, L.; Beaunier, P.; Remita, H. Bimetallic palladium−gold nanostructures: application in ethanol oxidation. *Chem. Mater.* **2009**, *21*, 3677−3683.

(8) Moskovits, M. Surface roughness and the enhanced intensity of Raman scattering by molecules adsorbed on metals. *J. Chem. Phys.* **1978**, *69*, 4159−4161.

(9) King, F. W.; Van Duyne, R. P.; Schatz, G. C. Theory of Raman scattering by molecules adsorbed on electrode surfaces. *J. Chem. Phys.* **1978**, *69*, 4472−4481.

(10) Schatz, G. C.; Van Duyne, R. P. Image field theory of enhanced Raman scattering by molecules adsorbed on metal surfaces: detailed comparison with experimental results. *Surf. Sci.* **1980**, *101*, 425−438.

(11) Khurgin, J. B. How to deal with the loss in plasmonics and metamaterials. *Nat. Nanotechnol.* **2015**, *10*, 2−6.

(12) Narang, P.; Sundararaman, R.; Atwater, H. A. Plasmonic hot carrier dynamics in solid-state and chemical systems for energy conversion. *Nanophotonics* **2016**, *5*, 96−111.

(13) Manjavacas, A.; Liu, J. G.; Kulkarni, V.; Nordlander, P. Plasmon-induced hot carriers in metallic nanoparticles. *ACS Nano* **2014**, *8*, 7630−7638.
(14) Joplin, A.; Hosseini Jebeli, S. A.; Sung, E.; Diemler, N.; Straney, P. J.; Yorulmaz, M.; Chang, W.-S.; Millstone, J. E.; Link, S. Correlated absorption and scattering spectroscopy of individual platinum-decorated gold nanorods reveals strong excitation enhancement in the nonplasmonic metal. *ACS Nano* **2017**, *11*, 12346−12357.
(15) Brown, A. M.; Sundararaman, R.; Narang, P.; Goddard, W. A., III; Atwater, H. A. Nonradiative plasmon decay and hot carrier dynamics: effects of phonons, surfaces, and geometry. *ACS Nano* **2015**, *10*, 957−966.
(16) Hartland, G. V. Optical studies of dynamics in noble metal nanostructures. *Chem. Rev.* **2011**, *111*, 3858−3887.
(17) Ma, J.; Wang, Z.; Wang, L.-W. Interplay between plasmon and single-particle excitations in a metal nanocluster. *Nat. Commun.* **2015**, *6*, 10107.
(18) Cortés, E.; Xie, W.; Cambiasso, J.; Jermyn, A. S.; Sundararaman, R.; Narang, P.; Schlücker, S.; Maier, S. A. Plasmonic hot electron transport drives nano-localized chemistry. *Nat. Commun.* **2017**, *8*, 14880.
(19) Kazuma, E.; Jung, J.; Ueba, H.; Trenary, M.; Kim, Y. Real-space and real-time observation of a plasmon-induced chemical reaction of a single molecule. *Science* **2018**, *360*, 521−526.
(20) Wang, F.; Li, C.; Chen, H.; Jiang, R.; Sun, L.-D.; Li, Q.; Wang, J.; Yu, J. C.; Yan, C.-H. Plasmonic harvesting of light energy for Suzuki coupling reactions. *J. Am. Chem. Soc.* **2013**, *135*, 5588−5601.
(21) Lou, Z.; Fujitsuka, M.; Majima, T. Pt−Au triangular nanoprisms with strong dipole plasmon resonance for hydrogen generation studied by single-particle spectroscopy. *ACS Nano* **2016**, *10*, 6299−6305.
(22) Swearer, D. F.; Robatjazi, H.; Martirez, J. M. P.; Zhang, M.; Zhou, L.; Carter, E. A.; Nordlander, P.; Halas, N. J. Plasmonic photocatalysis of nitrous oxide into N2 and O2 using aluminum-iridium antenna-reactor nanoparticles. *ACS Nano* **2019**, *13*, 8076−8086.
(23) Li, Z.; Kurouski, D. Elucidation of photo-catalytic properties of gold-platinum bimetallic nanoplates using tip-enhanced Raman spectroscopy. *J. Phys. Chem. C* **2020**, *124*, 12850−12854.
(24) Li, Z.; Wang, R.; Kurouski, D. Nanoscale photocatalytic activity of gold and gold-palladium nanostructures revealed by tip-enhanced Raman spectroscopy. *J. Phys. Chem. Lett.* **2020**, *11*, 5531−5537.
(25) Sonntag, M. D.; Klingsporn, J. M.; Garibay, L. K.; Roberts, J. M.; Dieringer, J. A.; Seideman, T.; Scheidt, K. A.; Jensen, L.; Schatz, G. C.; Van Duyne, R. P. Single molecule tip enhanced Raman spectroscopy. *J. Phys. Chem. C* **2012**, *116*, 478−483.
(26) Zhang, R.; Zhang, Y.; Dong, Z. C.; Jiang, S.; Zhang, C.; Chen, L. G.; Zhang, L.; Liao, Y.; Aizpurua, J.; Luo, Y.; et al. Chemical mapping of a single molecule by plasmon-enhanced Raman scattering. *Nature* **2013**, *498*, 82−86.
(27) Kurouski, D. Advances of tip-enhanced Raman spectroscopy (TERS) in electrochemistry, biochemistry, and surface science. *Vib. Spectrosc.* **2017**, *91*, 3−15.
(28) Lee, J.; Crampton, K. T.; Tallarida, N.; Apkarian, V. A. Visualizing vibrational normal modes of a single molecule with atomically confined light. *Nature* **2019**, *568*, 78−82.
(29) Kurouski, D.; Mattei, M.; Van Duyne, R. P. Probing redox reactions at the nanoscale with electrochemical tip-enhanced Raman spectroscopy. *Nano Lett.* **2015**, *15*, 7956−7962.
(30) Becker, S. F.; Esmann, M.; Yoo, K.; Gross, P.; Vogelgesang, R.; Park, N.; Lienau, C. Gap-plasmon-enhanced nanofocusing near-field microscopy. *ACS Photonics* **2016**, *3*, 223−232.
(31) Deckert-Gaudig, T.; Kurouski, D.; Hedegaard, M. A.; Singh, P.; Lednev, I. K.; Deckert, V. Spatially resolved spectroscopic differentiation of hydrophilic and hydrophobic domains on individual insulin amyloid fibrils. *Sci. Rep.* **2016**, *6*, 33575.
(32) Deckert-Gaudig, T.; Taguchi, A.; Kawata, S.; Deckert, V. Tip-enhanced Raman spectroscopy - from early developments to recent advances. *Chem. Soc. Rev.* **2017**, *46*, 4077−4110.
(33) Kurouski, D.; Deckert-Gaudig, T.; Deckert, V.; Lednev, I. K. Structure and composition of insulin fibril surfaces probed by TERS. *J. Am. Chem. Soc.* **2012**, *134*, 13323−13329.
(34) Kurouski, D.; Postiglione, T.; Deckert-Gaudig, T.; Deckert, V.; Lednev, I. K. Amide I vibrational mode suppression in surface (SERS) and tip (TERS) enhanced Raman spectra of protein specimens. *Analyst* **2013**, *138*, 1665−1673.
(35) Richard-Lacroix, M.; Zhang, Y.; Dong, Z.; Deckert, V. Mastering high resolution tip-enhanced Raman spectroscopy: towards a shift of perception. *Chem. Soc. Rev.* **2017**, *46*, 3922−3944.
(36) Treffer, R.; Böhme, R.; Deckert-Gaudig, T.; Lau, K.; Tiede, S.; Lin, X.; Deckert, V. Advances in TERS (tip-enhanced Raman scattering) for biochemical applications. *Biochem. Soc. Trans.* **2012**, *40*, 609−614.
(37) Wood, B. R.; Bailo, E.; Khiavi, M. A.; Tilley, L.; Deed, S.; Deckert-Gaudig, T.; McNaughton, D.; Deckert, V. Tip-enhanced Raman scattering (TERS) from hemozoin crystals within a sectioned erythrocyte. *Nano Lett.* **2011**, *11*, 1868−1873.
(38) van Schrojenstein Lantman, E. M.; Deckert-Gaudig, T.; Mank, A. J. G.; Deckert, V.; Weckhuysen, B. M. Catalytic processes monitored at the nanoscale with tip-enhanced Raman spectroscopy. *Nat. Nanotechnol.* **2012**, *7*, 583−586.
(39) Yin, H.; Zheng, L.-Q.; Fang, W.; Lai, Y.-H.; Porenta, N.; Goubert, G.; Zhang, H.; Su, H.-S.; Ren, B.; Richardson, J. O.; et al. Nanometre-scale spectroscopic visualization of catalytic sites during a hydrogenation reaction on a Pd/Au bimetallic catalyst. *Nat. Catal.* **2020**, *3*, 834−842.
(40) Zhong, J.-H.; Jin, X.; Meng, L.; Wang, X.; Su, H.-S.; Yang, Z.-L.; Williams, C. T.; Ren, B. Probing the electronic and catalytic properties of a bimetallic surface with 3 nm resolution. *Nat. Nanotechnol.* **2017**, *12*, 132−136.
(41) Wang, R.; Kurouski, D. Elucidation of tip-broadening effect in tip-enhanced Raman spectroscopy (TERS): a cause of artifacts or potential for 3D TERS. *J. Phys. Chem. C* **2018**, *122*, 24334−24340.
(42) Marr, J. M.; Schultz, Z. D. Imaging electric fields in SERS and TERS using the vibrational Stark effect. *J. Phys. Chem. Lett.* **2013**, *4*, 3268−3272.
(43) Kwasnieski, D. T.; Wang, H.; Schultz, Z. D. Alkyl-nitrile adlayers as probes of plasmonically induced electric fields. *Chem. Sci.* **2015**, *6*, 4484−4494.
(44) Banik, M.; El-Khoury, P. Z.; Nag, A.; Rodriguez-Perez, A.; Guarrottxena, N.; Bazan, G. C.; Apkarian, V. A. Surface-enhanced Raman trajectories on a nano-dumbbell: transition from field to charge transfer plasmons as the spheres fuse. *ACS Nano* **2012**, *6*, 10343−10354.
(45) Wang, R.; Li, J.; Rigor, J.; Large, N.; El-Khoury, P. Z.; Rogachev, A. Y.; Kurouski, D. Direct experimental evidence of hot-carrier-driven chemical processes in tip-enhanced Raman spectroscopy (TERS). *J. Phys. Chem. C* **2020**, *124*, 2238−2244.
(46) Bhattarai, A.; Cheng, Z.; Joly, A. G.; Novikova, I. V.; Evans, J. E.; Schultz, Z. D.; Jones, M. R.; El-Khoury, P. Z. Tip-Enhanced Raman Nanospectroscopy of Smooth Spherical Gold Nanoparticles. *J. Phys. Chem. Lett.* **2020**, *11*, 1795−1801.
(47) Wang, C.-F.; Cheng, Z.; O'Callahan, B. T.; Crampton, K. T.; Jones, M. R.; El-Khoury, P. Z. Tip-Enhanced Multipolar Raman Scattering. *J. Phys. Chem. Lett.* **2020**, *11*, 2464−2469.
(48) Bhattarai, A.; Crampton, K. T.; Joly, A. G.; Wang, C.-F.; Schultz, Z. D.; El-Khoury, P. Z. A Closer Look at Corrugated Au Tips. *J. Phys. Chem. Lett.* **2020**, *11*, 1915−1920.
(49) El-Khoury, P. Z.; Schultz, Z. D. From SERS to TERS and Beyond: Molecules as Probes of Nanoscopic Optical Fields. *J. Phys. Chem. C* **2020**, *124*, 27267−27275.
(50) Andrews, S. S.; Boxer, S. G. Vibrational Stark effects of nitriles I. methods and experimental results. *J. Phys. Chem. A* **2000**, *104*, 11853−11863.
(51) Bhattarai, A.; El-Khoury, P. Z. Nanoscale chemical reaction imaging at the solid−liquid interface via TERS. *J. Phys. Chem. Lett.* **2019**, *10*, 2817−2822.

https://dx.doi.org/10.1021/acs.jpcc.1c00155
J. Phys. Chem. C 2021, 125, 2492−2501

(52) Langhammer, C.; Yuan, Z.; Zorić, I.; Kasemo, B. Plasmonic properties of supported Pt and Pd nanostructures. *Nano Lett.* **2006**, *6*, 833−838.

https://dx.doi.org/10.1021/acs.jpcc.1c00155
J. Phys. Chem. C 2021, 125, 2492−2501